Journal of Power Sources 365 (2017) 362–371

Contents lists available at ScienceDirect

Journal of Power Sources

journal homepage: www.elsevier.com/locate/jpowsour

Ultrahigh surface area meso/microporous carbon formed with self-template for high-voltage aqueous supercapacitors

Jie Yang, Jiangtao Hu, Min Zhu, Yan Zhao, Haibiao Chen*, Feng Pan**

School of Advanced Materials, Shenzhen Graduate School, Peking University, Shenzhen, 518055, China

HIGHLIGHTS

- The meso/microporous carbon (MC) is synthesized by a simple self-template method.
- The MC electrode exhibits excellent performance in capacitance and rate capability.
- Three neutral electrolytes are studied to enhance the energy density of capacitors.
- The maximum operating voltage is essentially restricted by the positive potential.
- The symmetric supercapacitors exhibit high energy densities in aqueous solutions.

GRAPHICAL ABSTRACT

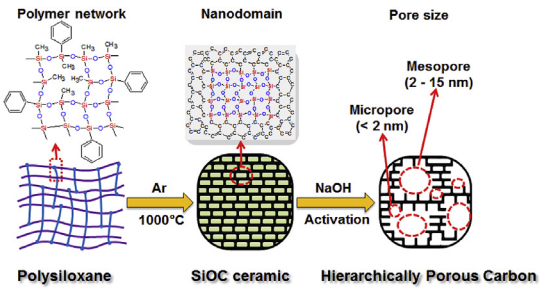

ARTICLE INFO

Article history:
Received 30 March 2017
Received in revised form
21 August 2017
Accepted 31 August 2017

Keywords:
Meso/microporous carbon
Aqueous supercapacitors
High-voltage
High energy density

ABSTRACT

A new hierarchically porous carbon has been synthesized with self-template of silica phase from a commercial silicone resin by pyrolysis and subsequent NaOH activation. The obtained carbon materials achieve an ultrahigh specific surface area (2896 m^2 g^{-1}) with abundant mesopores. The C800 sample demonstrates excellent performance in supercapacitors, with a high capacitance of 322 F g^{-1} at 0.5 A g^{-1} and outstanding rate capability (182 F g^{-1} at 100 A g^{-1}) in a three-electrode system using 6.0 mol L^{-1} KOH electrolyte. The energy density is improved by widening the voltage window using 1.0 mol L^{-1} alkali metal nitrate solutions ($LiNO_3$, $NaNO_3$, KNO_3) in which the strong solvation of alkali metal cations and nitrate anions effectively reduce the activity of water. In a symmetric supercapacitor, the maximum operating voltage is essentially restricted by the potential of positive electrode and the total capacitance is dominated by the capacitance of the anion at the positive electrode. The symmetric supercapacitors based on C800 deliver a high energy density of 22.4 Wh kg^{-1} at a power density of 0.23 kW kg^{-1} in 1.0 mol L^{-1} $LiNO_3$ with a voltage of 1.8 V and long-term stability with a retention of 89.87% after 10000 cycles.

1. Introduction

To meet the increasing demand for portable electronic devices and hybrid electric vehicles, supercapacitors based on porous carbons (electrical double-layer capacitors, or EDLCs) have received extensive attention owing to their advantages of high power

* Corresponding author.
** Corresponding author.
E-mail addresses: chenhb@pkusz.edu.cn (H. Chen), panfeng@pkusz.edu.cn (F. Pan).

http://dx.doi.org/10.1016/j.jpowsour.2017.08.114
0378-7753/

density and long cycle life compared with rechargeable batteries [1–3]. However, the wide application of supercapacitors has been hampered by their relatively low energy densities. The energy density of commercial supercapacitors based on traditional activated carbon is about 5 Wh kg^{-1}, which is much lower than that of lithium-ion batteries (about 100 Wh kg^{-1}) [4–6]. Therefore, considerable efforts have been devoted to increasing the energy density of supercapacitors without losing the high specific power and cycling stability.

It is well-known that the energy density of supercapacitors is proportional to the specific capacitance of the material and the square of the operating voltage ($E = 0.5\ CV^2$) [7,8]. To effectively increase the energy density of supercapacitors, extensive research has been carried out to increase the operating voltage. Generally, the electrochemical window is limited by the stability of the electrolytes. The operating voltage range is usually limited to 1.0 V in acidic and alkaline aqueous media, while the stability window of organic electrolytes is wider than 2.5 V [9]. However, organic electrolytes usually have low conductivity and high viscosity. Additionally, organic electrolytes are unfriendly to the environment and complicated to use due to their sensitivity to moisture. Hence, neutral aqueous media are considered as promising electrolytes from the viewpoint of application since they are cheap, environmentally friendly, non-corrosive and suitable for various current collectors. In recent years, neutral aqueous solutions such as sulfate and nitrate have attracted much interest due to relatively wider electrochemical window, which can be as wide as 1.6 V–2.0 V [9,10]. Widening of the electrochemical window in neutral aqueous solutions may be attributed to the strong solvation of ions and low concentration of protons or hydroxyl groups. However, large solvated ions migrate slower, especially in narrow pores, leading to declined rate capability.

Another important way to increase the energy density of supercapacitors is to develop new high performance materials with ultra-high effective surface area. Nowadays, new types of porous carbon materials with high specific surface area, excellent conductivity, low cost and environmental friendliness have been widely researched for energy storage and conversion applications especially for EDLCs [11,12]. Considering that the energy storage mechanism in EDLCs is based on ion adsorption at the electrode/electrolyte interface, the performance of EDLCs is largely determined by the specific surface area, pore structure of the carbon material and ion dimension [13–15]. In addition, introducing specific types of functional groups to the carbon surface would be beneficial for the electrolyte to access the carbon surface easily and may contribute some pseudo-capacitance [16]. Usually, porous carbon materials with a high specific surface area contain mostly micropores, and suffer from a poor rate performance due to sluggish ionic diffusion within the micropores [17,18]. Thus, it is important to develop hierarchically porous materials combining micropores with mesopores and macropores to improve the performance in terms of both capacitance and rate capability. Preparing hierarchically porous materials with different carbon sources by different method has been widely reported [5,19–21]. Macropores can play a role as reservoir to supply electrolyte ions from the bulk to the electrode/electrolyte interface, while mesopores can provide larger accessible surface area and serve as channels for fast ion transport, which will be beneficial for the accessibility of micropores [15,22]. Obtaining both a high specific surface area and a large proportion of mesopores in porous carbon materials often resorts to addition and subsequent removal of sacrificial templates, which complicates the synthesis process and raises the materials cost.

Recently, we developed a facile method to produce meso/microporous carbon material from a polysiloxane precursor using a traditional activation process. The new carbon material achieved an ultrahigh surface area and a large mesopore volume without using any additional templates. The polysiloxane precursor was prepared by addition polymerization under a platinum based catalyst [23]. In this work, we used commercial silicone resin as a precursor to produce nonporous SiOC ceramic followed by NaOH activation. The silica distributed in the framework of SiOC ceramic can function as a self-template to modulate hierarchically porous carbon formation with optimized pore structure. Different from our previous work, the silicone resin is a commercial product and it polymerizes through condensation without a platinum catalyst. Using commercial silicone resin further simplified the process and reduced the cost, and can potentially facilitate large scale production. The hierarchically porous carbon prepared from the commercial silicone resin achieved a specific surface area as high as 2896 $m^2\ g^{-1}$ and it contained micropores and mesopores. The porous carbon material showed high specific capacitance and outstanding rate capability (322 F g^{-1} at 0.5 A g^{-1} and 182 F g^{-1} at 100 A g^{-1}) in a three-electrode system. Moreover, the corresponding symmetric supercapacitor operated in 1.8 V exhibited an excellent stability (89.87% capacitance retention after 10000 cycles) and a high energy density of 22.4 Wh kg^{-1} in 1.0 M $LiNO_3$, which is much higher than most previously reported carbon-based symmetric supercapacitors in aqueous electrolytes.

2. Experimental

Synthesis of silicone resin derived carbon: The process for synthesizing the hierarchically porous carbon is shown in Scheme 1. A commercial silicone resin (Wacker SILRES 604) was heated to 1000 °C at a 5 °C min^{-1} ramp rate and held for 4 h under argon atmosphere, followed by cooling down to room temperature naturally. After pyrolysis the silicone resin was converted into a carbon-rich SiOC ceramic, which was then pulverized and ground to fine powders. Then the obtained powder was mixed with NaOH with a mass ratio of 1:4 in a nickel crucible. The mixture was heated to 700 °C, 800 °C and 900 °C at a 5 °C min^{-1} ramp rate and held for 1 h under argon atmosphere. The obtained product was washed with de-ionized water until the filtrate was neutral. The sample was finally dried at 120 °C in an oven. The dried samples were designated as C700, C800 and C900 according to the NaOH activation temperature.

Materials characterization: The crystal structure of the materials was characterized by X-ray diffraction (XRD) using a Bruker D8 Advance diffractometer with Cu-Kα radiation. Raman spectra were obtained using a Horiba modular Raman system with a diode laser with wavelength of 532 nm. Nitrogen absorption/desorption measurement was performed to characterize the pore structure on a Micromeritics ASAP 2020 analyzer. The specific surface area was derived by the Brunauer-Emmett-Teller (BET) model and the pore size distribution (PSD) was derived from a density functional theory (DFT) model. The morphology analysis of the samples was performed by scanning electron microscopy (SEM, ZEISS Supra 55) and transmission electron microscopy (TEM, FEI Tecnai G2 F30). An X-ray photoelectron spectrometer (ESCALAB 250XL) was used to investigate the surface chemical properties of the samples.

Electrochemical measurements: The working electrode consisted of active material, acetylene black, and PTFE binder with a mass ratio of 8:1:1. The mixture was rolled into sheets with a uniform thickness of 100–150 μm and cut into slices of 1 cm in diameter. Then the slices were dried in a vacuum oven at 110 °C overnight and pressed onto a piece of titanium mesh as the working electrode. The mass of the active material in each working electrode was about 1.2–1.5 mg. The three-electrode tests were carried out in an aqueous solution (6.0 M KOH) with Pt electrode as the counter electrode and Hg/HgO electrode as the reference

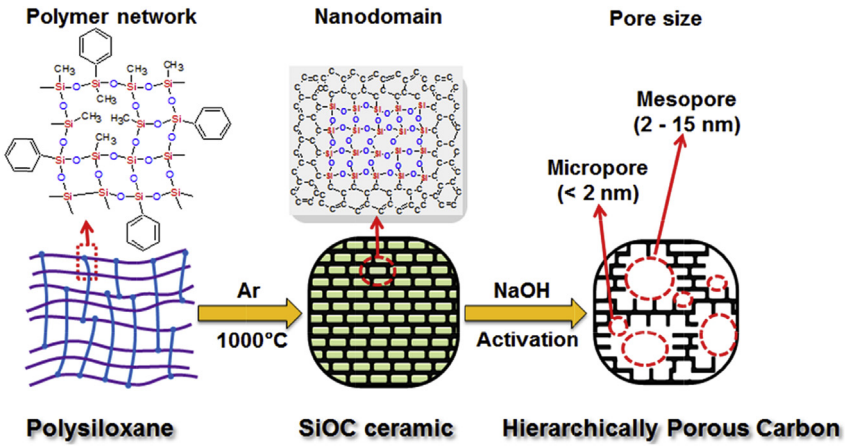

Scheme 1. Schematic illustration of the synthesis of hierarchically porous carbon from silicone resin.

electrode. For the two-electrode test, a symmetrical supercapacitor was assembled by stacking two identical electrode plates with a Whatman separator in between and 6.0 M KOH aqueous solution as the electrolyte in a CR2032 coin cell. Additionally, aqueous solutions of 1.0 M nitrate ($LiNO_3$, $NaNO_3$, KNO_3) were adopted to achieve a higher energy density. The cyclic voltammetry (CV) curves and electrochemical impedance spectroscopy (EIS) were obtained by a CHI660 electrochemical workstation (Shanghai Chenhua Instrument). The galvanostatic charge-discharge tests were carried out on a Maccor MC16 battery testing system.

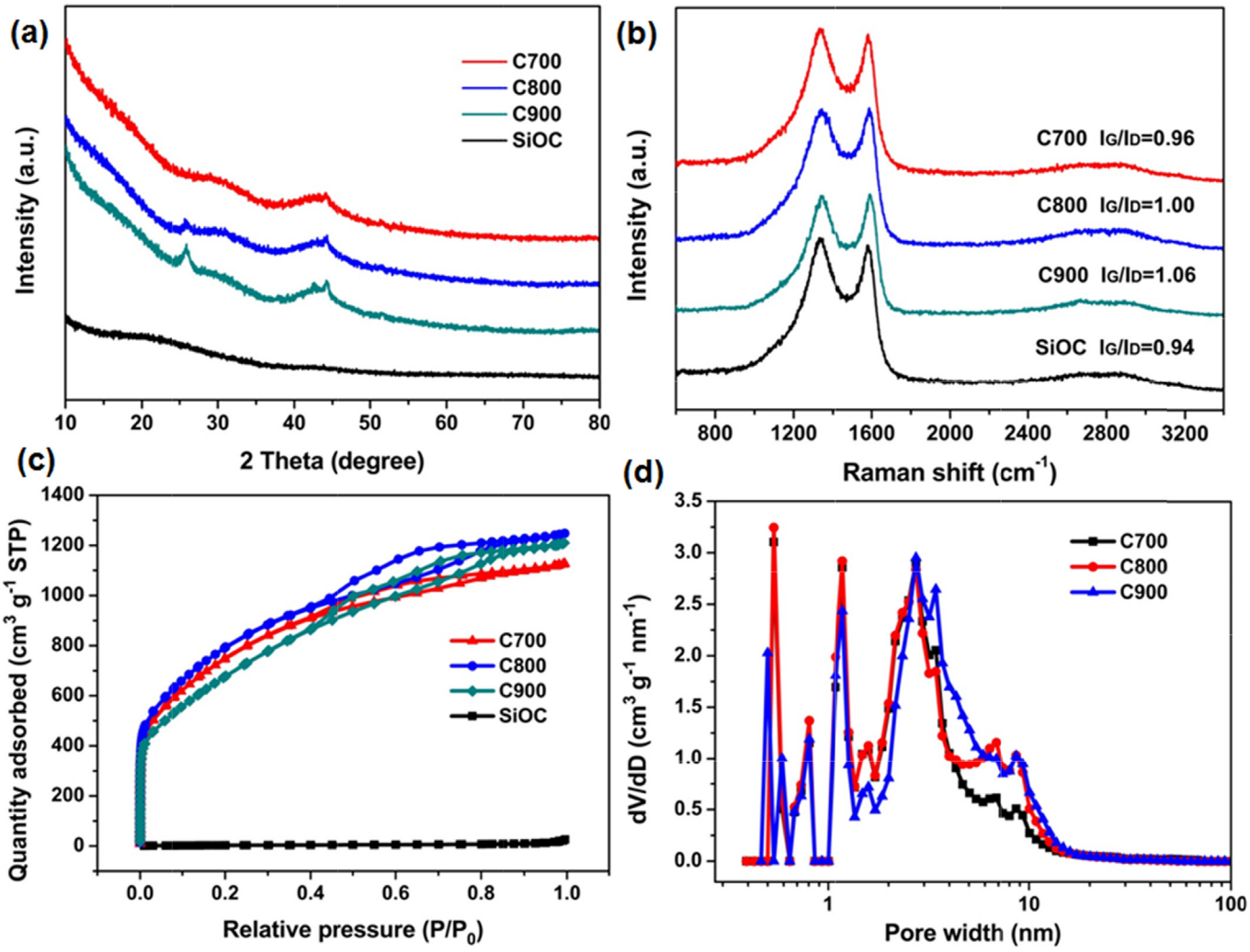

Fig. 1. (a) XRD patterns, (b) Raman spectra, (c) Nitrogen absorption/desorption isotherms and (d) DFT pore size distributions.

According to the discharging curve, the gravimetric capacitance (C) was calculated by the following equation:

$$C = \frac{I\Delta t}{\Delta V \mathrm{m}} \quad (1)$$

where I (A) represents the discharge current, Δt (s) represents the discharge time and ΔV (V) represents the potential range. m (g) is the mass of the active material of a single electrode in a three-electrode system, while m (g) is the total mass of the active material of both electrodes in a symmetric supercapacitor.

The corresponding energy density E (Wh kg^{-1}) and power density P (W kg^{-1}) were calculated by the equations as follows:

$$E = \frac{1}{2}C(\Delta V)^2 \quad (2)$$

$$P = \frac{E}{\Delta t} \quad (3)$$

where C (F g^{-1}) represents the gravimetric capacitance of the symmetrical supercapacitor, ΔV (V) represents the operating voltage, and Δt (h) represents the discharging time.

3. Results and discussion

The XRD patterns of SiOC ceramic and samples synthesized at different temperatures are shown in Fig. 1a. There are no obvious peaks observed in the SiOC ceramic, indicating its highly amorphous structure. As to the porous carbon samples, the two relatively broad peaks located at about 25.9° and 43.3° can be ascribed to the (002) and (101) planes of the graphitic carbon, which reflects the incomplete graphitization of the samples. The relatively high intensity in the low angle range can be attributed to the presence of abundant pores in the as-prepared porous carbon materials [6]. It is noted that the peaks at 25.9° and 43.3° become more pronounced with the temperature increasing, indicating the reduced structural defects and improved degree of graphitization.

The structures of samples were further investigated by the Raman spectra, shown in Fig. 1b. It can be found that the D-band is located at ~1350 cm^{-1}, which is caused by the breathing mode vibration [24]. And the G-band at ~1592 cm^{-1} can be attributed to the in-plane stretching mode vibration [25]. The ratio of the G-band intensity to the D-band intensity (I_G/I_D) is usually used to compare the ordered structure of carbon materials [26]. The relatively low ratios of I_G/I_D reveal the highly disordered structure in all the samples, which can be ascribed to the abundant pores existing in the carbon materials due to the alkaline activation. In addition, it is

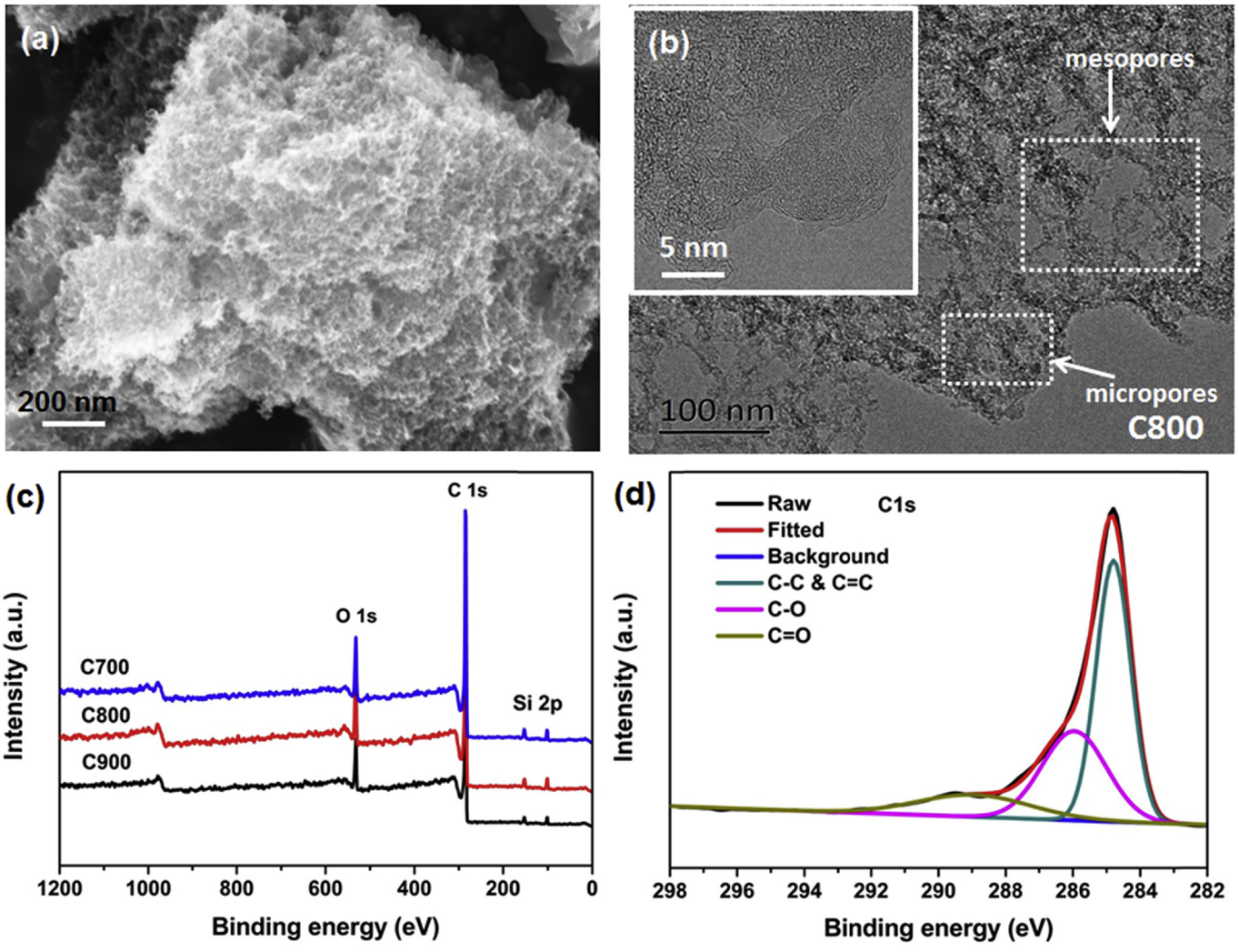

Fig. 2. (a) SEM image of C800, (b) TEM image of C800, (c) XPS spectra and (d) High resolution C 1s XPS spectrum of C800.

noted that the ratio of I_G/I_D shows an upward trend, indicating the improved degree of graphitization at higher temperature. Generally, the relatively high degree of graphitization would be beneficial to improve the conductivity and thereby facilitates the charge transfer.

The specific surface areas and pore size of the samples were analyzed by N_2 isothermal adsorption-desorption measurements. As shown in Fig. 1c, the specific surface area of SiOC ceramic was calculated to be about 10 $m^2 g^{-1}$, indicating that the SiOC ceramic is nonporous. As to the isotherms of samples, they display an evident hysteresis loop in the relative pressure (P/P_0) range from 0.41 to 0.85 due to the presence of mesopores. The corresponding specific surface areas of C700, C800 and C900 were calculated to be 2743 $m^2 g^{-1}$, 2896 $m^2 g^{-1}$ and 2502 $m^2 g^{-1}$, respectively. Generally, the relatively high specific surface area would increase the effective surface for the electrostatic attraction of ions. Based on the DFT model, the pore size distributions (PSD) of the samples are derived to be from 0.4 nm to 15 nm, which reveals that there are abundant micropores and mesopores coexisting in the samples, shown in Fig. 1d. It is believed that the hierarchical architecture of porous materials can take full advantage of the characteristics of different pores. Micropores can provide relatively high surface area for electrostatic adsorption of electrolyte ions, while mesopores can play a vital role in facilitating the infiltration and transport of electrolyte ions [15,27,28]. So the pore characteristics of our prepared materials should be beneficial in EDLC application.

The morphology of the samples was further observed by SEM and TEM. As shown in Fig. 2a, the typical morphology of C800 is cottony or cavernous with abundant interconnected pores. TEM (Fig. 2b) reveals the highly disordered and porous structure of C800. Additionally, X-ray photoelectron spectroscopy (XPS) was performed to investigate the element compositions of the samples, and the results are shown in Fig. 2c. The XPS results show that the samples mainly consist of C (87.53 at.%) and O (10.45 at.%) with a small amount of Si (2.02 at.%). As shown in Fig. 2d, the high-resolution C1s can be deconvoluted to three peaks, which are the C-C/C=C (~284.8 eV), C-O (~286.0 eV) and C=O (~288.9 eV) bonds, respectively [29–31]. The presence of abundant O-dopants in the prepared materials would lead to better wettability of the electrode and even some pseudocapacitance [13,32,33].

The electrochemical properties of the obtained samples were first investigated in a three-electrode system with 6.0 M KOH aqueous electrolyte. The cyclic voltammetry (CV) test of different samples were carried out at various scanning rates, shown in Fig. 3a and Fig. S2. As shown in Fig. 3a, CV curves of C800 display a quasi-rectangular shape and overlap at different scanning rates, suggesting a typical EDLC behavior and superior rate capability. Additionally, the corresponding galvanostatic charge/discharge (C/

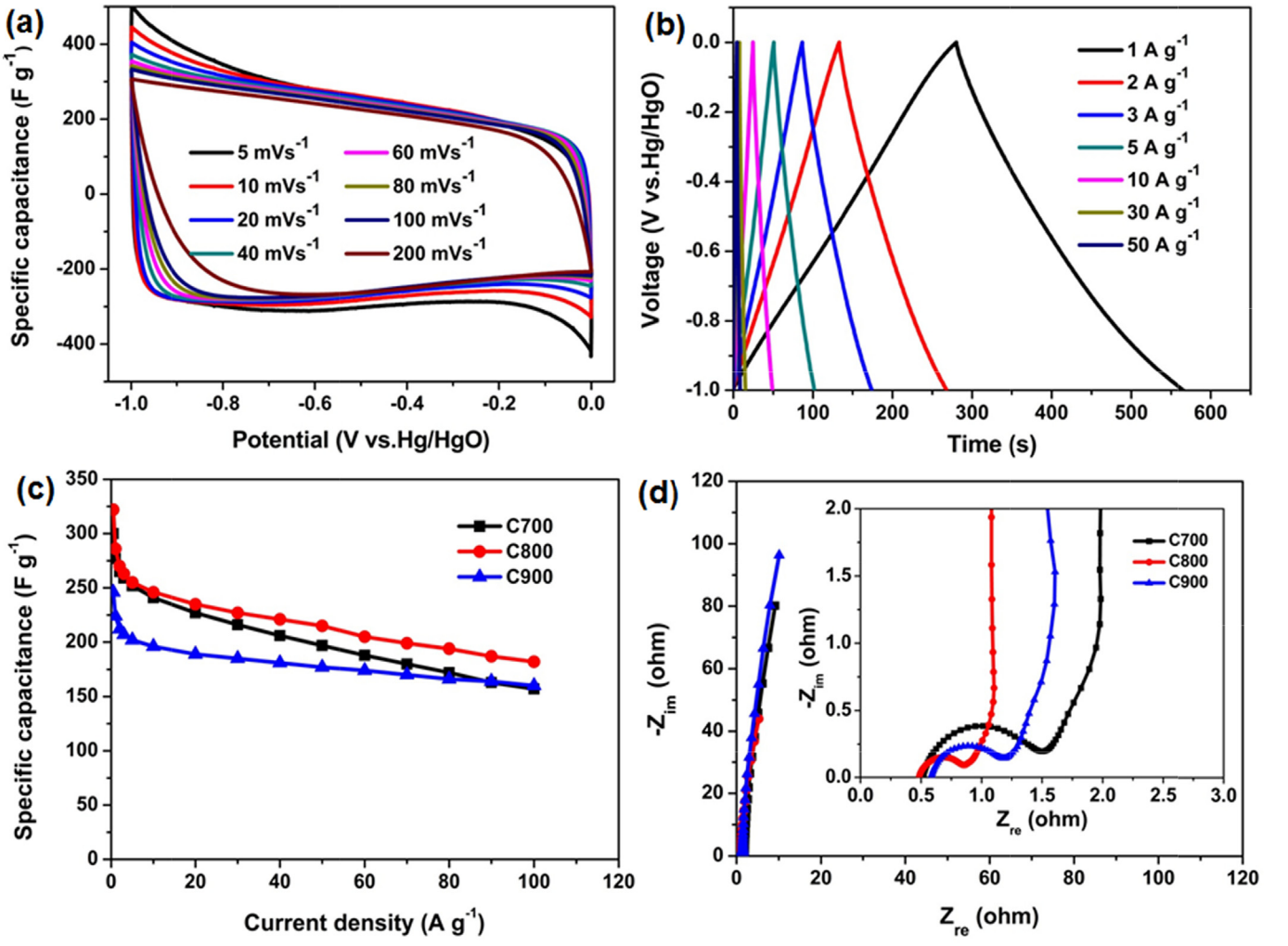

Fig. 3. Electrochemical characterizations in a three-electrode system with 6.0 M KOH: (a) cyclic voltammograms of C800, (b) galvanostatic charge-discharge curves of C800, (c) the specific capacitances of C700, C800 and C900 electrodes at various current densities and (d) Nyquist plots of C700, C800 and C900.

D) curves are symmetric triangle with a quite small IR drop (Fig. 3b). For example, the IR drop is about 0.10 V at 30 A g^{-1}. It is noted that C800 shows relatively higher capacitance and much better rate capability among the three samples, suggesting efficient mass and charge transfer in the C800 (e.g., 322 F g^{-1} at 0.5 A g^{-1} and 182 F g^{-1} at 100 A g^{-1}), shown in Fig. 3c. The high gravimetric capacitance of 182 F g^{-1} achieved at 100 A g^{-1} for C800 is much higher than those of many carbon materials [17,34–36]. Compared with C700, the specific surface area of C800 was slightly higher. Therefore, the specific capacitances of C700 and C800 were almost the same at a low current density because the electrical double-layer capacitance is highly dependent on the accessible surface area. The area-normalized specific capacitance of our materials was within 10–11 μF cm^{-2} at 0.5 A g^{-1} as shown in Fig. S3. However, when the current density was increased, the difference between C800 and C700 was enlarged due to the difference in mass transfer resistance. The total volume of mesopores was larger in C800 than in C700 (Table S1), and there were more mesopores in the range of 5–10 nm in C800 as visible in Fig. 1d. When the activation temperature was further increased to 900 °C, the specific surface area of C900 started to decrease because of the collapse of the pore structure. Although C900 also contained a large volume of mesopores and it demonstrated better rate performance than C700, its relatively low specific surface area resulted in a low specific capacitance. Therefore, C800 was believed to be the optimum among the three samples and the excellent performance of C800 was the result of both a high specific surface area and an optimal pore structure.

The kinetics of ion and charge transport were further revealed by electrochemical impedance spectroscopy (EIS), shown in Fig. 3d. The Nyquist plots indicate that all samples exhibit a nearly ideal capacitive behavior with a semicircle at the high frequency region and a straight line at the low frequency region [36,37]. The C800 has a relatively smaller intrinsic resistance of 0.48 Ω compared to those of C700 (0.52 Ω) and C900 (0.59 Ω). In addition, compared with C700 and C900, C800 shows a smaller semicircle in the high frequency region, indicating a faster charge-transfer. Furthermore, the C800 exhibits a nearly vertical slope at the low-frequency region, suggesting a low diffusion resistance and an ideal capacitance behavior.

To further evaluate the performance of C800 in the practical device, symmetrical two-electrode supercapacitors based on the same mass and size were also fabricated in CR2032 coin cells. The CV curves of the capacitor based on C800 display quasi-rectangular shapes without obvious distortion at various scanning rates (Fig. 4a), suggesting a typical EDLC behavior and excellent rate

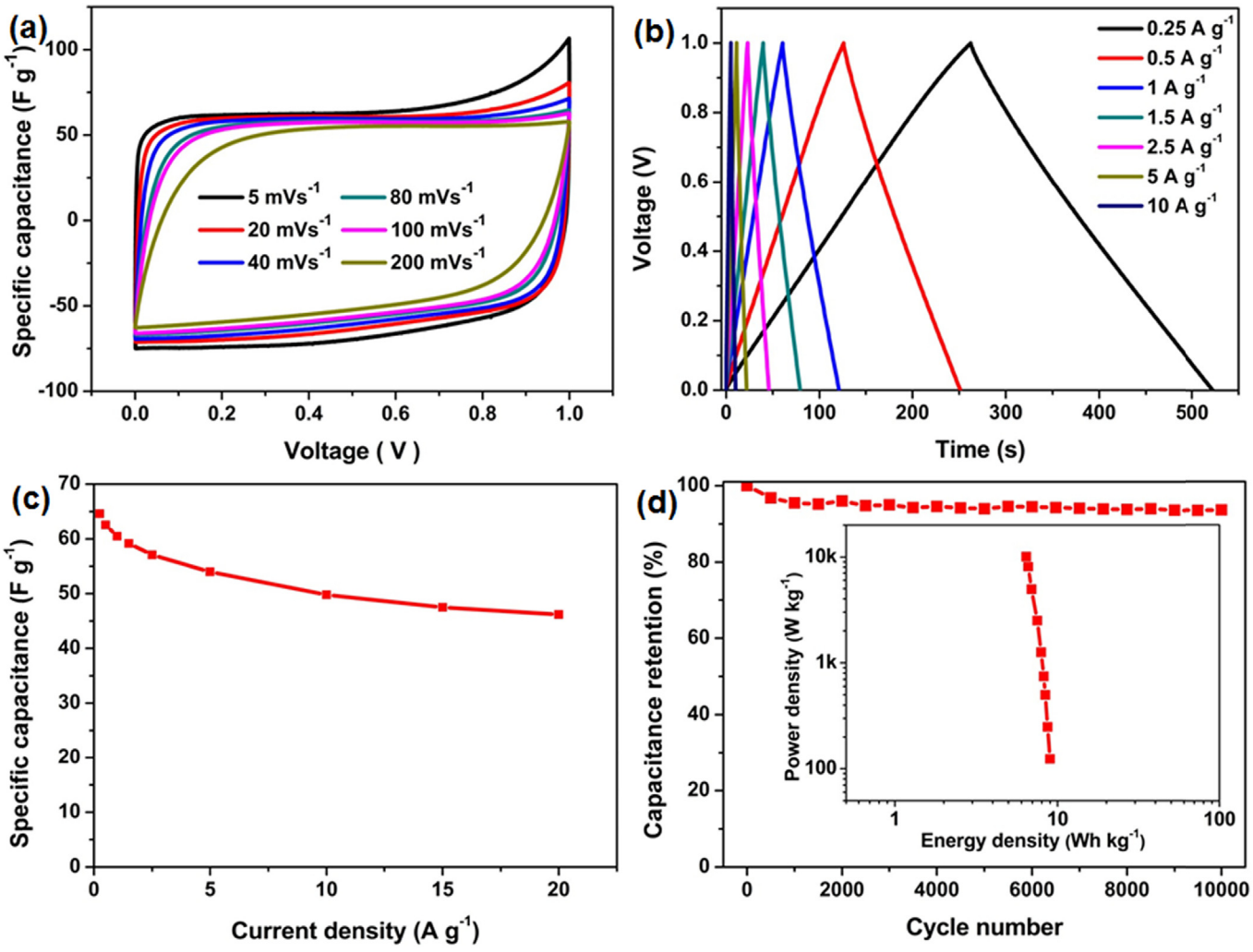

Fig. 4. Electrochemical characterizations carried out in a symmetrical two-electrode system with 6.0 M KOH: (a) CV curves of C800, (b) galvanostatic charge-discharge curves of C800, (c) the specific capacitances of C800 at various current densities and (d) cycling stability of C800 at 5 A g^{-1} and the inset of (d) shows the corresponding Ragone plot.

capability. As shown in Fig. 4b, the corresponding galvanostatic charge/discharge curves exhibit a highly symmetric triangular shape, indicating an ideal capacitive behavior and good reversibility. Fig. 4c shows the rate capability of C800 at various current densities. The capacitance based on C800 was calculated to be 64.62 F g^{-1} at 0.25 A g^{-1} and kept a high retention rate of 71.5% (46.21 F g^{-1}) at 20 A g^{-1}. The high specific capacitance and outstanding rate capability of C800 can be mainly ascribed to the relatively high specific surface area and fast ion transmission by optimized pore structure. As shown in Fig. 4d, the supercapacitor based on C800 also showed excellent cycling stability with a high retention of 93.3% after 10,000 C/D cycles at a current density of 5 A g^{-1}. The corresponding Ragone plot is shown in the inset of Fig. 4d, which exhibits a high energy density of 8.96 Wh kg^{-1} at a power density of 124.31 W kg^{-1} and achieves a high power density of 10.09 kW kg^{-1} at an energy density of 6.42 Wh kg^{-1}.

According to the formula $E = 0.5\ CV^2$, increasing the operating voltage is the most effective way to increase the energy stored in a supercapacitor. To further enhance the energy density of the supercapacitors, neutral aqueous electrolytes have been adopted since some of them show broadened electrochemical window even beyond 2 V [37–40]. Additionally, they are non-flammable, non-corrosive, eco-friendly and highly conductive. As shown in Fig. 5a, the CV curves of C800 electrode were recorded in a three-electrode system with 1.0 M $LiNO_3$ as the electrolyte. According to the Nernst equation, cathodic potential limit for oxygen evolution reaction and anodic potential limit for hydrogen evolution reaction are 0.718 V and −0.512 V (vs Hg/HgO), respectively, at pH 7. However, the practical potential range is much larger than 1.23 V due to the overpotentials for the evolution of H_2 and O_2 [41]. It is noted that when the potential is higher than 1.1 V or lower than −1.1 V (vs Hg/HgO), the water begins to dramatically decompose. Based on the result of the CV, the relatively stable potential window of C800 electrode was preliminarily considered as about 2.0 V in a 1.0 M $LiNO_3$ aqueous electrolyte. Fig. 5b compares the electrochemical window of three different aqueous electrolytes. It indicates that there are no obvious differences among them in the potential range of −1.1 V to 1.1 V (vs Hg/HgO). It can be attributed to the slight difference in the hydrated ionic radii of the cations, which are 3.82 Å (Li^+), 3.58 Å (Na^+) and 3.31 Å (K^+), respectively [28,42]. The extended potential window can be attributed to the decreased activity of water, which mainly caused by the strong solvation of alkali metal cations and nitrate anions [28,37].

When it comes to a practical supercapacitor, it is impossible to

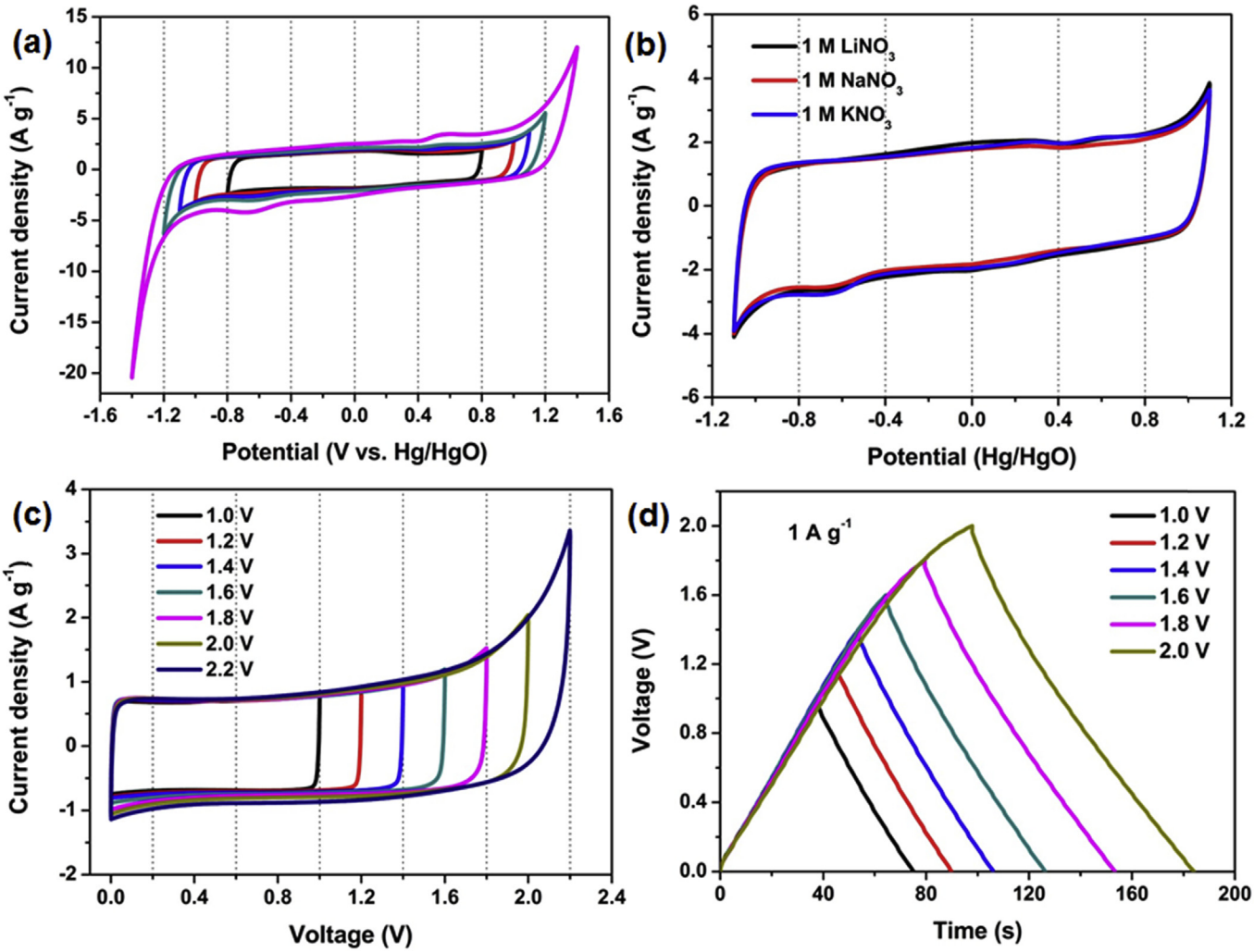

Fig. 5. (a) Cyclic voltammograms of C800 at 10 mV s^{-1} in a three-electrode system with 1.0 M $LiNO_3$, (b) comparison of electrochemical window in different aqueous electrolytes, (c) cyclic voltammograms of C800 at 10 mV s^{-1} in a two-electrode system with 1.0 M $LiNO_3$ and (d) galvanostatic charge-discharge characteristics (1 A g^{-1}) at different voltage ranges in a two-electrode system with 1.0 M $LiNO_3$.

regulate the potential of each electrode in a two-electrode configuration. So the available maximum cell voltage cannot be accurately determined by the stable potential window revealed in a three-electrode system. The available maximum cell voltage was further investigated in a two-electrode system. CV tests were firstly carried out in different ranges to confirm the stable electrochemical window, shown in Fig. 5c and Fig. S4. The CV tests of C800 symmetric supercapacitor with 1.0 M $LiNO_3$ were performed in various voltage ranges at 10 mV s^{-1}, shown in Fig. 5c. It is noted that the shape of CV curves still keep quasi-rectangular without evident rising of the current in the range from 1.0 to 1.8 V. However, as the voltage is further increased to 2.0 V, the current exhibits an obvious upward trend due to the discernible contribution of faradaic current probably derived from the oxidation of carbon surface groups or the decomposition of electrolyte [43,44]. The stable electrochemical window was further confirmed by galvanostatic charge-discharge curves, shown in Fig. 5d. When the cell voltage is increased to 2.0 V, obvious distortion of the linearity is observed, which is caused by pseudo-capacitive effect. So the stable and practical electrochemical window should be in the range of 0–1.8 V in the 1.0 M $LiNO_3$ aqueous electrolyte, which can be attributed to the strong solvation of lithium ion and nitrate ion [28,45]. In other words, strong solvation of ions with high hydration energy allows water to stably exist at the voltage of 1.8 V in the 1.0 M $LiNO_3$ aqueous electrolyte.

To investigate which electrode limited the operating voltage, the potential range of each electrode was separately monitored by using an Hg/HgO reference electrode during the process of charge and discharge in the two-electrode test. Fig. 6a shows the potential range of each electrode when a given voltage was imposed on the supercapacitor. It is noted that when the cell was applied with a high voltage of 2.0 V, the potential of the positive electrode was already beyond the stable and practical potential limit, while the potential of the negative electrode was still far from the corresponding limit. Consequently, the maximum operating voltage is essentially restricted by the potential of the positive electrode.

It is well known that the double-layer capacitor is based on charge storage at the electrode/electrolyte interface. The corresponding capacitances of anion (C_-) and cation (C_+) at the positive and negative electrodes, respectively, have also been calculated by Equation (1), shown in Fig. 6b. It is noted that the capacitance of each electrode depends on the type of adsorbed ions in a symmetric supercapacitor. The capacitance of the cation (C_+) at the negative electrode is much higher than that of the anion (C_-) at the positive electrode. It can be attributed to difference in the size of the anions and cations because the size of ions can influence the

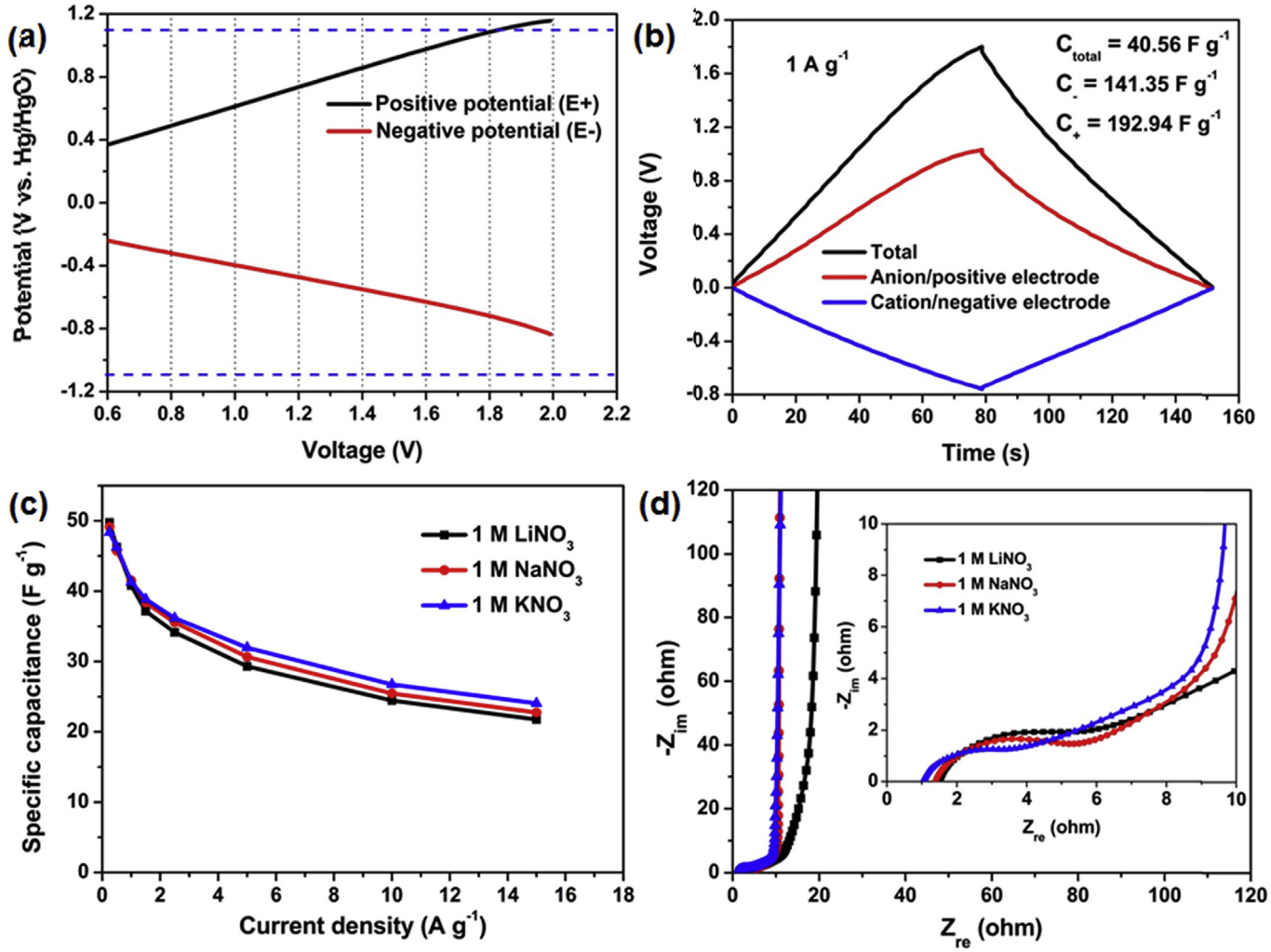

Fig. 6. Tests carried out in a two-electrode system: (a) Potential changes of the positive and negative electrodes in 1.0 M $LiNO_3$, (b) the specific capacitances of the anion/positive electrode (C_-) and cation/negative electrode (C_+) in 1.0 M $LiNO_3$ at 1 A g^{-1}, (c) the specific capacitances at different current densities and (d) Nyquist spectra.

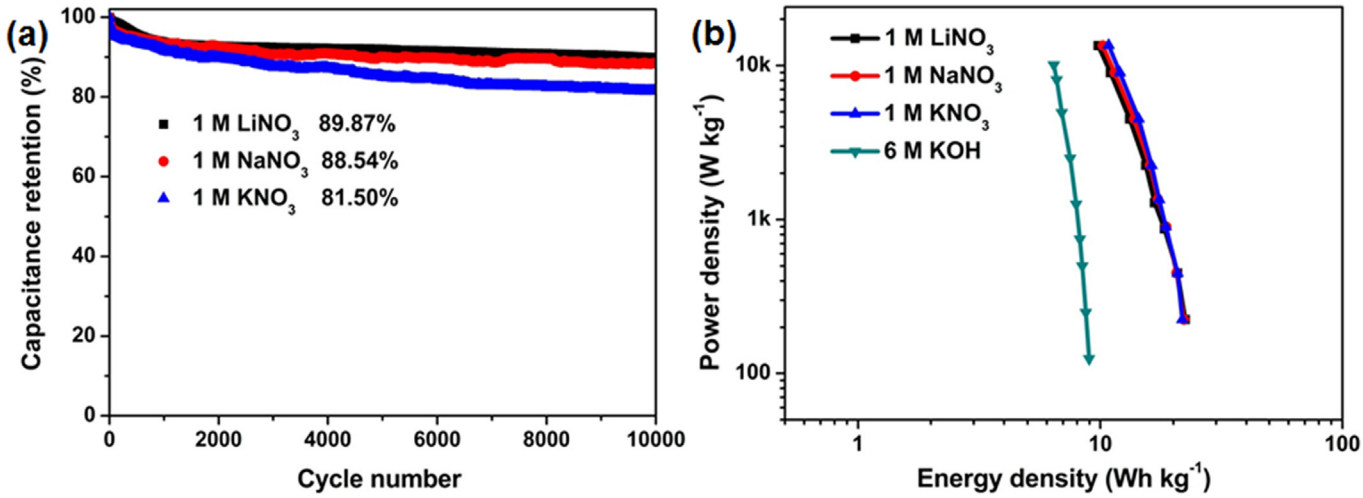

Fig. 7. (a) Cycling stability of symmetric supercapacitors based on C800 electrodes at 2.5 A g^{-1} and (b) Ragone plots of symmetric supercapacitors based on C800 electrodes in aqueous electrolytes.

effective thickness of the electrical double-layer. Since an EDLC composes a serial connection of the (negative electrode)/electrolyte interface and the electrolyte/(positive electrode) interface, the capacitance of an EDLC is determined by the electrode with a smaller capacitance value. Hence, the maximum capacitance of the symmetric supercapacitor is dominated by the capacitance of the anion (C_-) at the positive electrode in 1.0 M $LiNO_3$. Similar results were also observed in the 1.0 M $NaNO_3$ and 1.0 M KNO_3, shown in Fig. S7.

The symmetric supercapacitors were further tested at various charge/discharge current densities within 0–1.8 V window. The corresponding results tested in the three different alkali metal nitrate solutions are shown in Fig. 6c. With the current densities increasing, the capacitance values show a downtrend in the three aqueous electrolytes. The capacitance retention is about 50% as the current density increases from 0.5 A g^{-1} to 15 A g^{-1}. The slowest attenuation of the capacitance in 1.0 M KNO_3 can be attributed to the smallest hydrated ionic radius of K^+, which means that it is much easier for K^+ than Na^+ and Li^+ to enter the inner pores of the materials. Fig. 6d shows the Nyquist plots of capacitors based on C800 electrodes in different electrolytes. The Nyquist plots exhibit a typical capacitive shape, which is made up of a semicircle at mid-high frequencies and a nearly vertical line at low frequencies. The intercept on the real axis is 1.04 Ω for 1.0 M KNO_3, which is slightly lower than that for 1.0 M $NaNO_3$ (1.40 Ω) and 1.0 M $LiNO_3$ (1.51 Ω). It directly verifies that the conductivity of KNO_3 is the best among them. The sequence of the diameters of the semicircles is in the order of $LiNO_3$ > $NaNO_3$ > KNO_3, which means K^+ owns the highest ionic diffusion rate. These results are in good agreement with the corresponding rate capability.

Additionally, the stability of the supercapacitor based on C800 was tested at 2.5 A g^{-1} with a voltage of 1.8 V in the different alkali metal nitrate solutions, shown in Fig. 7a. The excellent cycling stability proves that the operating voltage of 1.8 V is applicable and good stability of the as-prepared material. Fig. 7b shows the Ragone plots for the symmetric EDLCs operated at 1.8 V in different aqueous electrolytes. The energy and power densities were calculated based on the mass of active materials in both electrodes. There are slight differences in the energy density and power density among the three different aqueous electrolytes. The maximum energy density up to 22.4 Wh kg^{-1} was achieved at a power density of 0.23 kW kg^{-1} in 1.0 M $LiNO_3$ and the maximum power density of 13.53 kW kg^{-1} was obtained at an energy density of 10.82 Wh kg^{-1}. The excellent performance is among the highest level of reported carbon-based symmetric supercapacitors in aqueous media (see Table S2) [22,45–53]. It suggests that our hierarchically porous carbon materials have a promising prospect applied in high-voltage aqueous supercapacitors.

4. Conclusions

In summary, we have developed a simple method to synthesize ultrahigh specific surface area carbon materials with hierarchically porous structure using silica domains as a self-template in SiOC ceramic. It was demonstrated that the optimal C800 material exhibited high capacitance (322 F g^{-1} at 0.5 A g^{-1}) and excellent rate capacity with a retention of 56.52% (182 F g^{-1}) at current density of 100 A g^{-1} tested in a three-electrode system. The outstanding capacitive performance can be ascribed to the ultrahigh specific surface area and easily accessible pore architecture. Furthermore, the symmetric supercapacitor based on C800 showed a high energy density of 22.4 Wh kg^{-1} and good stability tested in 1.0 M $LiNO_3$ electrolyte with an operating voltage of 1.8 V. The maximum operating voltage was essentially restricted by the potential of the positive electrode and the total capacitance was dominated by the capacitance of the anion at the positive electrode. The energy density achieved by the C800 material is significantly higher than those previously reported in carbon-based symmetric supercapacitors in aqueous solutions. It suggests that our hierarchically porous carbon would be potentially a promising material for high performance supercapacitors applied in aqueous electrolyte, considering the alkali metal nitrate solutions are non-flammable, non-corrosive and eco-friendly.

Acknowledgements

This research was financially supported by the National Materials Genome Project (2016YFB0700600), the Guangdong Innovation Team Project (No. 2013N080), and the Shenzhen Science and Technology Research Grants (Nos. JCYJ20150626110958181, JCYJ20150518092933435, JCYJ20170412150450297).

Appendix A. Supplementary data

Supplementary data related to this article can be found at http://dx.doi.org/10.1016/j.jpowsour.2017.08.114.

References

[1] P. Simon, Y. Gogotsi, Nat. Mater 7 (2008) 845–854.
[2] J.R. Miller, P. Simon, Science 321 (2008) 651–652.
[3] A. Burke, J. Power Sources 91 (2000) 37–50.
[4] Y. Zhu, S. Murali, M.D. Stoller, K.J. Ganesh, W. Cai, P.J. Ferreira, A. Pirkle, R.M. Wallace, K.A. Cychosz, M. Thommes, Science 332 (2011) 1537–1541.
[5] Y. Jin, K. Tian, L. Wei, X. Zhang, X. Guo, J. Mater. Chem. A 4 (2016) 15968–15979.
[6] J. Xu, Z. Tan, W. Zeng, G. Chen, S. Wu, Y. Zhao, K. Ni, Z. Tao, M. Ikram, H. Ji, Adv. Energy. Mater 28 (2016), 5331–5331.
[7] E. Frackowiak, Phys. Chem. Chem. Phys. 9 (2007) 1774–1785.
[8] V. Khomenko, E. Raymundo-Piñero, F. Béguin, J. Power Sources 195 (2010) 4234–4241.
[9] Q. Gao, L. Demarconnay, E. Raymundo-Piñero, F. Béguin, Energy Environ. Sci. 5 (2012) 9611–9617.
[10] E. Mora, C. Blanco, R. Santamaría, M. Granda, R. Menéndez, Carbon 41 (2003) 445–452.
[11] Y. Li, Z.Y. Fu, B.L. Su, Adv. Funct. Mater 22 (2012) 4634–4667.
[12] Y. Zhai, Y. Dou, D. Zhao, P.F. Fulvio, R.T. Mayes, S. Dai, Adv. Mater 23 (2011) 4828–4850.
[13] Q. Li, R. Jiang, Y. Dou, Z. Wu, T. Huang, D. Feng, J. Yang, A. Yu, D. Zhao, Carbon 49 (2011) 1248–1257.
[14] J. Wei, D. Zhou, Z. Sun, Y. Deng, Y. Xia, D. Zhao, Adv. Funct. Mater 23 (2013) 2322–2328.
[15] Y. Gong, Z. Wei, J. Wang, P. Zhang, H. Li, Y. Wang, Sci. Rep. 4 (2014), 6349–6349.
[16] D. Lozano-Castelló, J.P. Marco-Lozar, M.J. Bleda-Martínez, F. Montilla, E. Morallón, A. Linares-Solano, D. Cazorla-Amorós, Carbon 57 (2013) 41–47.
[17] Q. Long, W. Chen, H. Xu, X. Xiong, Y. Jiang, F. Zou, X. Hu, Y. Xin, Z. Zhang, Y. Huang, Energy Environ. Sci. 6 (2013) 2497–2504.
[18] J. Zhang, L. Jin, J. Cheng, H. Hu, Carbon 55 (2013) 221–232.
[19] J. Hu, H. Wang, X. Huang, Electrochim. Acta 74 (2012) 98–104.
[20] Z. Chen, D. Weng, H. Sohn, M. Cai, Y. Lu, Rsc Adv. 2 (2012) 1755–1758.
[21] Y. Li, Z. Li, P.K. Shen, Adv. Mater 25 (2013) 2474–2480.
[22] Q. Wang, J. Yan, Y. Wang, T. Wei, M. Zhang, X. Jing, Z. Fan, Carbon 67 (2014) 119–127.
[23] J. Yang, H. Wu, M. Zhu, W. Ren, Y. Lin, H. Chen, F. Pan, Nano Energy 33 (2017) 453–461.
[24] G.N. Yushin, E.N. Hoffman, A. Nikitin, H. Ye, M.W. Barsoum, Y. Gogotsi, Carbon 43 (2005) 2075–2082.
[25] Y. Korenblit, M. Rose, E. Kockrick, L. Borchardt, A. Kvit, S. Kaskel, G. Yushin, ACS nano 4 (2010) 1337–1344.
[26] A.C. Ferrari, J. Robertson, Phys. Rev. B Condens. Matter 61 (2000) 14095–14107.
[27] D.W. Wang, F. Li, M. Liu, G.Q. Lu, H.M. Cheng, Angew. Chem. 47 (2008) 373–376.
[28] K. Fic, G. Lota, M. Meller, E. Frackowiak, Energy Environ. Sci. 5 (2012) 5842–5850.
[29] T.I.T. Okpalugo, P. Papakonstantinou, H. Murphy, J. Mclaughlin, N. Brown, Carbon 43 (2004) 153–161.
[30] Y. Li, Y. Zhao, H. Cheng, Y. Hu, G. Shi, L. Dai, L. Qu, J. Am. Chem. Soc. 134 (2011) 15–18.
[31] Y.S. Yun, S. Lee, N.R. Kim, M. Kang, C. Leal, K.Y. Park, K. Kang, H.J. Jin, Y.S. Yun, S. Lee, J. Power Sources 313 (2016) 142–151.
[32] I.Y. Jeon, S.Y. Bae, J.M. Seo, J.B. Baek, Adv. Funct. Mater 25 (2015) 6961–6975.
[33] X.M. Feng, R.M. Li, Y.W. Ma, R.F. Chen, N.E. Shi, Q.L. Fan, W. Huang, Adv. Funct. Mater 21 (2011) 2989–2996.
[34] P. Cheng, T. Li, H. Yu, L. Zhi, Z. Liu, Z. Lei, J. Phys. Chem. C 120 (2016) 2079–2086.
[35] W. Tian, Q. Gao, Y. Tan, K. Yang, L. Zhu, C. Yang, H. Zhang, J. Mater. Chem. A 3 (2015) 5656–5664.
[36] J. Hao, Y. Liao, Y. Zhong, D. Shu, C. He, S. Guo, Y. Huang, J. Zhong, L. Hu, Carbon 94 (2015) 879–887.
[37] M.P. Bichat, E. Raymundo-Piñero, F. Béguin, Carbon 48 (2010) 4351–4361.
[38] L. Demarconnay, E. Raymundo-Piñero, F. Béguin, Electrochem. Commun. 12 (2010) 1275–1278.
[39] J.H. Chae, G.Z. Chen, Electrochim. Acta 86 (2012) 248–254.
[40] H. Luo, Y. Yang, B. Mu, Y. Chen, J. Zhang, X. Zhao, Carbon 100 (2016) 214–222.
[41] L. Suo, O. Borodin, T. Gao, M. Olguin, J. Ho, X. Fan, C. Luo, C. Wang, K. Xu, Science 350 (2015) 938–943.
[42] Q.T. Qu, B. Wang, L.C. Yang, Y. Shi, S. Tian, Y.P. Wu, Electrochem. Commun. 10 (2008) 1652–1655.
[43] B. Avasarala, R. Moore, P. Haldar, Electrochim. Acta 55 (2010) 4765–4771.
[44] M. He, K. Fic, P. Novák, E.J. Berg, Energy Environ. Sci. 9 (2015) 623–633.
[45] G. Hasegawa, K. Kanamori, T. Kiyomura, H. Kurata, T. Abe, K. Nakanishi, Chem. Mater 28 (2016) 3944–3950.
[46] J. Zhao, H. Lai, Z. Lyu, Y. Jiang, K. Xie, X. Wang, Q. Wu, L. Yang, Z. Jin, Y. Ma, Adv. Mater 27 (2015) 3541–3545.
[47] W. Qian, J. Zhu, Z. Ye, W. Xiao, Y. Feng, Small 11 (2015) 4959–4969.
[48] L. Sun, Y. Fu, C. Tian, Y. Yang, L. Wang, J. Yin, J. Ma, R. Wang, H. Fu, ChemSusChem 7 (2014) 1637–1646.
[49] X. Fan, C. Yu, J. Yang, Z. Ling, C. Hu, M. Zhang, J. Qiu, Adv. Energy. Mater 5 (2015) 1401761–1401767.
[50] E.Y.L. Teo, L. Muniandy, E.P. Ng, F. Adam, A.R. Mohamed, R. Jose, K.F. Chong, Electrochim. Acta 192 (2016) 110–119.
[51] C. Long, X. Chen, L. Jiang, L. Zhi, Z. Fan, Nano Energy 12 (2015) 141–151.
[52] H. Zhu, X. Wang, F. Yang, X. Yang, Adv. Mater 23 (2011) 2745–2748.
[53] Q. Wang, J. Yan, T. Wei, J. Feng, Y. Ren, Z. Fan, M. Zhang, X. Jing, Carbon 60 (2013) 481–487.